MULTI-FIDELITY DESIGN OPTIMIZATION OF AXISYMMETRIC BODIES IN INCOMPRESSIBLE FLOW

Leifur Leifsson, Slawomir Koziel and Stanislav Ogurtsov
Engineering Optimization & Modeling Center, School of Science and Engineering, Reykjavik University
Menntavegur 1, 101 Reykjavik, Iceland

Keywords: Axisymmetric body, Underwater vehicles, Hydrodynamic shape optimization, CFD, Direct design, Inverse design, Surrogate modelling.

Abstract: The paper discusses multi-fidelity design optimization of axisymmetric bodies in incompressible fluid flow. The algorithm uses a computationally cheap low-fidelity model to construct a surrogate of an accurate but CPU-intensive high-fidelity model. The low-fidelity model is based on the same governing equations as the high-fidelity one, but exploits coarser discretization and relaxed convergence criteria. The low-fidelity model is corrected by aligning the hull surface pressure and skin friction distributions with the corresponding distributions of the high-fidelity model using a multiplicative response correction. Our approach can be implemented in both direct and inverse design approaches. Results of two case studies for hull drag minimization and target pressure distribution matching show that optimized designs are obtained at substantially lower computational cost (over 94%) when compared to the direct high-fidelity model optimization.

1 INTRODUCTION

Autonomous underwater vehicles (AUVs) are becoming increasingly important in various marine applications, such as oceanography, pipeline inspection, and mine counter measures (Yamamoto, 2007). Endurance (speed and range) is one of the more important attribute of AUVs (Allen et al., 2000). Vehicle drag reduction and/or an increase in the propulsion system efficiency will translate to a longer range for a given speed (or the same distance in a reduced time). A careful hydrodynamic design of the AUVs, including the hull shape, the protrutions, and the propulsion system, is therefore essential.

The fluid flow around an underwater vehicle with appendages is characterized by flow features such as thick boundary layers, vortices and turbulent wakes generated due to the hull and the appendages (Huang et al., 1992). These flow features can have adverse effects on, for example, the performance of the propulsion system and the control planes. Moreover, the drag depends highly on the vehicle shape, as well as on the aforementioned flow features. For that reason, it is important to account for these effects during the design of the AUVs.

The prediction of the flow past the full three-dimensional configuration of the AUVs requires the use of computational fluid dynamics (CFD). Numerous applications of CFD methods to the flow past AUVs and other underwater vehicles are in the literature, e.g., Yang and Löhner, 2003; Barros et al. 2008; and Jagadeesh et al., 2009. The purpose of these investigations is to predict properties such as added masses, pressure and friction distributions, drag, normal force and moment coefficients, wake field, and stability derivatives. Comparison with experimental measurements show that CFD is reliable and can yield accurate results (Yang and Löhner, 2003; Barros et al. 2008; and Jagadeesh et al., 2009).

Numerous studies on underwater vehicle design and optimization have been reported which focus on the clean hull only, i.e., the appendages and the propulsion system are neglected and the flow is taken to be past an axisymmetric body at a zero angle of attack. Examples of such numerical studies include Goldschmied (1966), Parsons et al. (1974), Myring (1976), Dalton and Zedan (1980), Lutz and Wagner (1998), Alvarez et al. (2009), and Solov'ev (2009). Allen et al. (2000), however, report an

Leifsson L., Koziel S. and Ogurtsov S..
MULTI-FIDELITY DESIGN OPTIMIZATION OF AXISYMMETRIC BODIES IN INCOMPRESSIBLE FLOW.
DOI: 10.5220/0003646104650473
In *Proceedings of 1st International Conference on Simulation and Modeling Methodologies, Technologies and Applications* (SDDOM-2011), pages 465-473
ISBN: 978-989-8425-78-2

experimental investigation of propulsion system enhancements and drag reduction of an AUV.

The hydrodynamic design optimization of AUVs in full configuration, taking into account the appendages and the propulsion system, is still an open problem. One of the main challenges involved is the high computational cost of a CFD simulation. A single CFD simulation of the three-dimensional flow past an AUV can take a few hours up to several days, depending on the computational power, the grid density, and the flow conditions. Therefore, the direct optimization can be impractial, especially using traditional gradient-based methods.

An important research area in the field of aerodynamic optimization is focused on employing the surrogate-based optimization (SBO) techniques (Queipo et al., 2005; Forrester and Keane, 2009). One of the major objectives is to reduce the number of high-fidelity model evaluations, and thereby making the optimization process more efficient. In SBO, the accurate, but computationally expensive, high-fidelity CFD simulations are replaced—in the optimization process—by a cheap surrogate model. SBO has been successfully applied to the aerodynamic design optimization of various aerospace components, such as airfoils (e.g., Leifsson and Koziel, 2010), aircraft wings (e.g., Alexandrov et al., 2000), and turbine blades (e.g., Braembussche, 2008).

The surrogate models can be created either by approximating the sampled high-fidelity model data using regression (so-called function approximation surrogates) (see for example Queipo et al., 2005), or by correcting physics-based low-fidelity models which are less accurate but computationally cheap representations of the high-fidelity models (see, e.g., Bandler et al., 2004, Alexandrov et al., 2000). The latter models are typically more expensive to evaluate. However, less high-fidelity model data is normally needed to obtain a given accuracy level. SBO with physics-based low-fidelity models is called multi- or variable-fidelity optimization.

In this paper, we present a hydrodynamic shape optimization methodology based on the SBO concept for AUVs. In particular, we adopt the multi-fidelity approach with the high-fidelity model based on the Reynolds-Averaged Navier-Stokes (RANS) equations, and the low-fidelity model based on the same equations, but with coarse discretization and relaxed convergence criteria. We use a simple response correction to create the surrogate. Here, we choose to focus on the clean hull design, which is a convenient case study to implement and test our design approach.

2 PROBLEM FORMULATION

We constrain the hull shapes to the most common AUV shape, namely, the torpedo shape, i.e., a three section axisymmetric body with a nose, a cylindrical midsection, and a tail. Typically, equipment such as the computer, sensors, electronics, batteries, and payload are housed in the nose and the midsection, whereas the propulsion system is in the tail. Figure 1 shows a typical torpedo shaped hull with a nose of length a, midsection of length b, overall length L, and maximum diameter of D.

2.1 Shape Parameterization

We parameterize the nose and the tail using Bézier curves (Lepine et al., 2001). The Bézier curve, of degree n, is defined as

$$B(t) = \sum_{k=1}^{m} \sum_{i=0}^{n} \frac{n!}{i!(n-i)!} (1-t(k))^{n-i} t(k)^{i} P(i), \quad (1)$$

where P_i, $i = 0 \ldots n$, are the control points, and t is an $1 \times m$ array from 0 to 1.

We use five control points for the nose and four for the tail, as shown in Fig. 2. Control points number three and eight are free (x- and y-coordinates), while the other points are fixed. We, therefore, have two design variables for the nose and tail curves, a total of four design variables, aside from the hull dimensions a, b, L, and D.

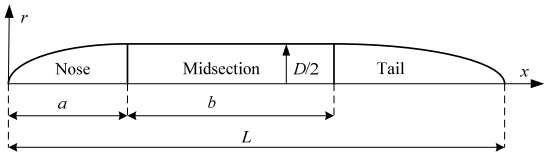

Figure 1: A sketch of a typical axisymmetric torpedo shaped hull form.

2.2 Design Approaches

The goal of hydrodynamic shape optimization is to find an optimal—with respect to given objectives—hull shape, so that given design constraints are satisfied. There are two main approaches two this problem. One is to adjust the hull geometrical shape to maximize performance. This is called direct design, and the most common design goal, when considering the clean hull, is drag minimization. An alternative approach is to define a priori a specific flow behavior that is to be attained. This is called inverse design, and, typically in hydrodynamic design, a target velocity distribution is prescribed

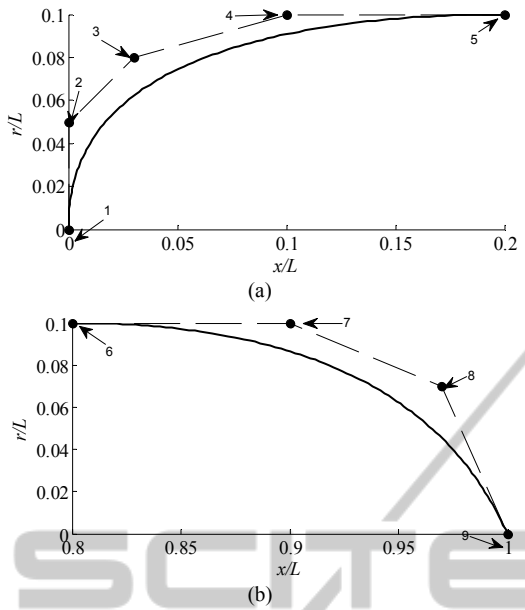

Figure 2: Bézier curves are used to represent the shapes of (a) the nose (5 control points); and (b) the tail (4 control points). Control points 3 and 8 are free, while the other points are essentially fixed (depend on L, a, b, and D).

(Dalton and Zedan, 1980). Instead, a target pressure distribution can be prescribed a priori, which is more common in aerodynamic design (Dulikravich, 1991). Typically, inverse design minimizes the norm of the difference between the target and design distributions. The main difficulty in this approach is to define the target distribution. In this paper we consider both the direct and the inverse design approaches.

3 COMPUTATIONAL MODELS

3.1 High-Fidelity CFD Model

The flow past the hull is considered to be steady and incompressible. The Reynolds-Averaged Navier-Stokes (RANS) equations are assumed as the governing flow equations with the two-equation k-ε turbulence model with standard wall functions (Tannehill et al., 1997).

The solution domain is axisymmetric around the hull centreline axis and extends two body lengths in front of the hull, five body lengths behind it, and two body lengths above it (Fig. 3). At the inlet, there is a velocity boundary condition where the velocity is set parallel to the hull axis, i.e., zero angle of attack. Pressure is prescribed at the outlet (zero gauge pressure).

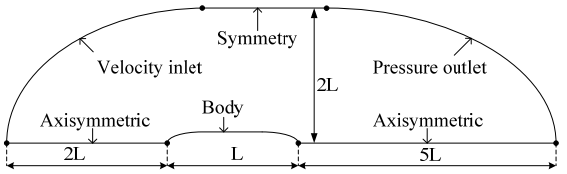

Figure 3: The computational solution domain and the boundary conditions.

The CFD computer code FLUENT (2006) is used for numerical simulations of the fluid flow. Asymptotic convergence to a steady state solution is obtained for each case. The iterative convergence of each solution is examined by monitoring the overall residual, which is the sum (over all the cells in the computational domain) of the L^2 norm of all the governing equations solved in each cell. In addition to this, the drag force (defined in Section 3.3) is monitored for convergence. A solution is considered converged if a residual value of 10^{-6} has been reached for all equations, or the number of iterations reaches 1000.

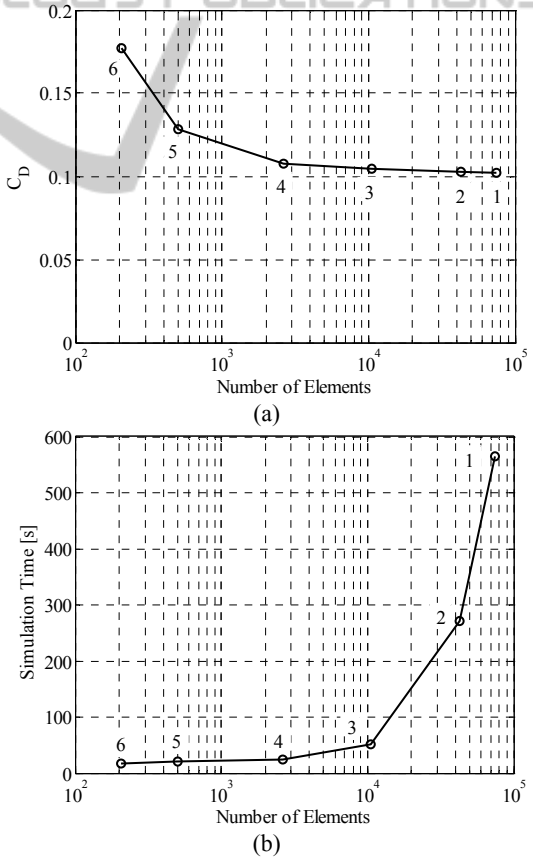

Figure 4: Grid convergence study at a speed of 2 m/s and Reynolds number of 2 million; (a) the change in the drag coefficient C_D (defined in Section 3.3) with the number of elements; (b) the variation in the simulation time with number of elements.

The computational grid is structured with quadrilateral elements. The elements are clustered around the body and grow in size with distance from the body. The grids are generated using ICEM CFD (2006). A grid convergence study was performed to determine the necessary grid density (Fig. 4). A torpedo shaped body with L/D = 5 was used in the study. The inlet speed was 2 *m/s* and the Reynolds number was 2 million. Clearly, the drag coefficient value has converged at the finest grids (number 1 and 2) (Fig. 4(a)). There is, however, a large difference in the simulation time between the two finest grids (Fig. 4(b)). Therefore, we selected grid number 2, with 42,763 elements, to use for the high-fidelity CFD model in the optimization process.

The velocity contours, pressure and skin friction distributions are shown in Figs. 5 and 6 for illustration purposes.

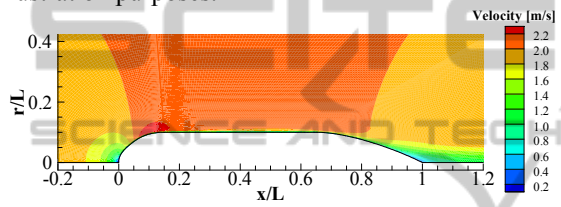

Figure 5: Velocity contours of the flow past an axisymmetric torpedo shape hull at 2 m/s and Reynolds number of 2 million. Grid 5 of Fig. 4 was used in the simulation.

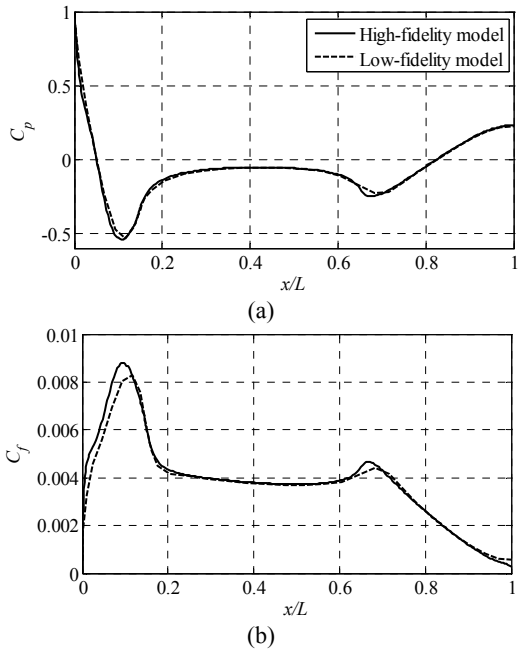

Figure 6: Flow distributions (from the high-fidelity and low-fidelity models (defined in Section 3.2)) on the hull surface of the flow shown in Fig. 5; (a) the pressure distribution; and (b) the skin friction distribution.

3.2 Low-Fidelity CFD Model

The low-fidelity model is based on the same CFD model as the high-fidelity one. However, as the low-fidelity model will be used in place of the high-fidelity model in the optimization process, it needs to be faster than the high-fidelity one. The simulation time is substantially reduced by making the grid coarser (Fig. 4(b)). Grid number 6 needs the lowest simulation time and is the least accurate. A closer look at that grid reveals that it is too coarse (the responses were too "grainy"). Consequently, we selected grid number 5, with 504 elements, to be used for the low-fidelity model.

The simulation time can be reduced further by reducing the number of iterations. Figure 7 shows how the drag coefficient reaches a converged value after approximately 50 iterations. We therefore relax the convergence criteria for the low-fidelity model by setting it to 50 iterations. The ratio of simulation time of the high-fidelity model to the low-fidelity model is around 15.

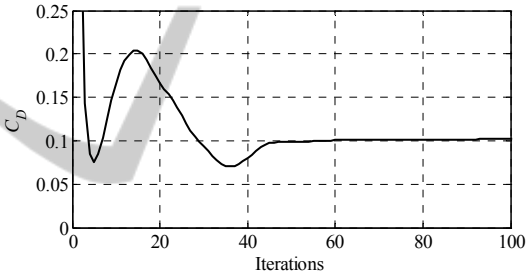

Figure 7: Variation of the drag coefficient with number of iterations for the case shown in Fig. 5.

3.3 Hull Drag Calculation

For a body in incompressible flow, the total drag is due to pressure and friction forces, which are calculated by integrating the pressure (C_p) and skin friction (C_f) distributions over the hull surface. The pressure coefficient is defined as $C_p \equiv (p-p_\infty)/q_\infty$, where p is the local static pressure, p_∞ is free-stream static pressure, and $q_\infty = (1/2\rho_\infty V_\infty^2)$ is the dynamic pressure, with ρ_∞ as the free-stream density, and the V_∞ free-stream velocity. The skin friction coefficient is defined as $C_f \equiv \tau/q_\infty$, where τ is the shear stress. Typical C_p and C_f distributions are shown in Fig. 6.

The total drag coefficient is defined as $C_D \equiv d/(q_\infty S)$, where d is the total drag force, and S is the reference area. Here, we use the frontal-area of the hull as the reference area. The drag coefficient is the sum of the pressure and friction drag, or

$$C_D = C_{Dp} + C_{Df}\,, \tag{2}$$

where C_{Dp} is the pressure drag coefficient and C_{Df} is the skin friction drag coefficient. The CFD analysis yields static pressure and wall shear stress values (which are non-dimensionalized to give C_p and C_f) at the element nodes (Fig. 8). The pressure acts normal to the surface and the shear stress parallel to it. The pressure drag coefficient is calculated by integrating from the leading-edge of the nose to the trailing-edge of the tail

$$C_{Dp} = 2\pi\int_0^L C_p(x)\sin\theta(x)r(x)\,dx\,, \tag{3}$$

where $C_p(x)$ is assumed to vary linear between the element nodes, $\theta(x)$ is angle of each element relative to the x-axis, and L is the length of the hull. Similarly, the skin friction drag coefficient is calculated as

$$C_{Df} = 2\pi\int_0^L C_f(x)\cos\theta(x)r(x)\,dx\,. \tag{4}$$

4 OPTIMIZATION PROCEDURE

4.1 Design Problem Formulation

Our design task is formulated as a nonlinear minimization problem of the form

$$\boldsymbol{x}^* = \arg\min_{\boldsymbol{l}\le\boldsymbol{x}\le\boldsymbol{u}} f(\boldsymbol{x}) \tag{5}$$

where $f(\boldsymbol{x})$ is the objective function, $\boldsymbol{x}$ is the design variable vector, whereas $\boldsymbol{l}$ and $\boldsymbol{u}$ are the lower and upper bounds, respectively. Here, no nonlinear constraints are present, the design variables are control parameters that parameterize the hull shape (cf. Section 2.1). The objective function depends on the particular design scenario. For direct design (see Section 2.2), the objective function is just a drag coefficient as defined in Section 3.3. For inverse design (see Section 2.2), the objective is defined as a norm of the difference between the current and the target pressure distributions.

4.2 Surrogate-based Optimization

The high-fidelity model evaluation is CPU-intensive so that solving the problem (5) directly, by plugging in the high-fidelity model into the optimization loop, may be impractical. Instead, we would like to exploit surrogate-based optimization (SBO) (Bandler et al., 2004; Queipo et al., 2005) that shifts the optimization burden into the computationally cheap surrogate, and, thus, allows us to solve (5) at a low computational cost.

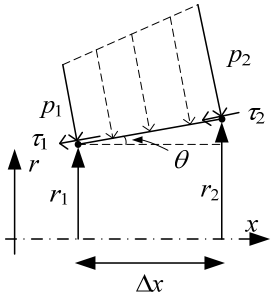

Figure 8: Edge of an element on the hull surface at radius r. The element length is Δx and it makes an angle θ to the x-axis. Pressure p acts normal to the hull surface. Shear stress τ acts parallel to the surface.

The generic SBO optimization scheme is the following

$$\boldsymbol{x}^{(i+1)} = \arg\min_{\boldsymbol{x}} s^{(i)}(\boldsymbol{x}) \tag{6}$$

where $\boldsymbol{x}^{(i)}$, i = 0, 1, ..., is a sequence of approximate solutions to (5), whereas $s^{(i)}$ is the surrogate model at iteration i. If the surrogate model is sufficiently good representation of the high-fidelity model f, the number of iterations required to find a satisfactory design is small (Koziel et al., 2006).

The surrogate model can be constructed either from sampled high-fidelity model data using an appropriate approximation technique (Simpson et al., 2001), or by utilizing a physically-based low-fidelity model (Bandler et al., 2004). Here, we exploit the latter approach as we have a reliable low-fidelity model at our disposal (see Section 3.2). Also, good physically-based surrogates can be constructed using a fraction of high-fidelity model data necessary to build accurate approximation models (Koziel and Bandler, 2010a).

There are several methods of constructing the surrogate from a physically-based low-fidelity model. They include, among others, space mapping (SM) (Bandler et al., 2004), various response correction techniques (Søndergaard, 2003), manifold mapping (Echeverría and Hemker, 2008), and shape-preserving response prediction (Koziel, 2010b). In this paper, the surrogate model is created using a simple multiplicative response correction, which turns out to be sufficient for our purposes. An advantage of such an approach is that the surrogate is constructed using a single high-fidelity model evaluation, and it is very easy to implement.

4.3 Surrogate Model Construction

Recall that $C_{p,f}(\boldsymbol{x})$ and $C_{f,f}(\boldsymbol{x})$ denote the pressure and

skin friction distributions of the high-fidelity model. The respective distributions of the low-fidelity model are denoted as $C_{p.c}(\boldsymbol{x})$ and $C_{f.c}(\boldsymbol{x})$. We will use the notation $C_{p.f}(\boldsymbol{x}) = [C_{p.f.1}(\boldsymbol{x})\ C_{p.f.2}(\boldsymbol{x})\ \ldots\ C_{p.f.m}(\boldsymbol{x})]^T$, where $C_{p.f.j}(\boldsymbol{x})$ is the jth component of $C_{p.f}(\boldsymbol{x})$, with the components corresponding to different coordinates along the x/L axis.

At iteration i, the surrogate model $C_{p.s}^{(i)}$ of the pressure distribution $C_{p.f}$ is constructed using the multiplicative response correction of the form:

$$C_{p.s}^{(i)}(\boldsymbol{x}) = [C_{p.s.1}^{(i)}(\boldsymbol{x})\ \ C_{p.s.2}^{(i)}(\boldsymbol{x})\ \ \ldots\ \ C_{p.s.m}^{(i)}(\boldsymbol{x})]^T \quad (7)$$

$$C_{p.s.j}^{(i)}(\boldsymbol{x}) = A_{p.j}^{(i)} \cdot C_{p.c.j}(\boldsymbol{x}) \quad (8)$$

$j = 1, 2, \ldots, m$, where

$$A_{p.j}^{(i)} = \frac{C_{p.f.j}^{(i)}(\boldsymbol{x}^{(i)})}{C_{p.c.j}^{(i)}(\boldsymbol{x}^{(i)})} \quad (9)$$

Similar definition holds for the skin friction distribution model $C_{f.s}^{(i)}$. Note that the formulation (7)-(9) ensures zero-order consistency (Alexandrov and Lewis, 2001) between the surrogate and the high-fidelity model, i.e., $C_{p.f}(\boldsymbol{x}^{(i)}) = C_{p.s}^{(i)}(\boldsymbol{x}^{(i)})$. Rigorously speaking, this is not sufficient to ensure the convergence of the surrogate-based scheme (6) to the optimal solution of (5). However, because of being constructed from the physically-based low-fidelity model, the surrogate (7)-(9) exhibits quite good generalization capability. As demonstrated in Section 5, this is sufficient for good performance of the surrogate-based design process.

One of the issues of model (7)-(9) is that (9) is not defined whenever $C_{p.c.j}(\boldsymbol{x}^{(i)})$ equals zero, and that the values of $A_{p.j}^{(i)}$ are very large when $C_{p.c.j}(\boldsymbol{x}^{(i)})$ is close to zero. This may be a source of substantial distortion of the surrogate model response as illustrated in Fig. 9. In order to alleviate this problem, the original surrogate model response is "smoothened" in the vicinity of the regions where $A_{p.j}^{(i)}$ is large (which indicates the problems mentioned above). Let $j_{\max}$ be such that $|A_{p.j\max}^{(i)}| >> 1$ assumes (locally) the largest value. Let Δj be the user-defined index range (typically, $\Delta j = 0.01 \cdot m$). The original values of $A_{p.j}^{(i)}$ are replaced, for $j = j_{\max}-\Delta j, \ldots, j_{\max}-1, j_{\max}, j_{\max}+1, \ldots, j_{\max}+\Delta j$, by the interpolated values:

$$\begin{aligned} \overline{A}_{p.j}^{(i)} = I(&\{[j_{\max} - 2\Delta j \ldots j_{\max} - \Delta j - 1] \cup \\ &\cup [j_{\max} + \Delta j - 1 \ldots j_{\max} + 2\Delta j]\}, \\ &\{[A_{p.j_{\max}-2\Delta j}^{(i)} \ldots A_{p.j_{\max}-\Delta j-1}^{(i)}] \cup \\ &\cup [A_{p.j_{\max}-2\Delta j}^{(i)} \ldots A_{p.j_{\max}-\Delta j-1}^{(i)}]\}, j) \end{aligned} \quad (10)$$

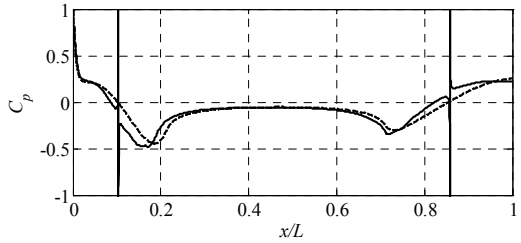

Figure 9: Surrogate model $C_{p.s}^{(i)}$ (7)-(9) at $\boldsymbol{x}^{(i)}$ (- - -), and at some other design $\boldsymbol{x}$ (—). By definition, $C_{p.s}^{(i)}(\boldsymbol{x}^{(i)}) = C_{p.f}(\boldsymbol{x}^{(i)})$. Note that $C_{p.s}^{(i)}(\boldsymbol{x})$ has large spikes around the points where $C_{p.s}^{(i)}(\boldsymbol{x}^{(i)})$ is close to zero.

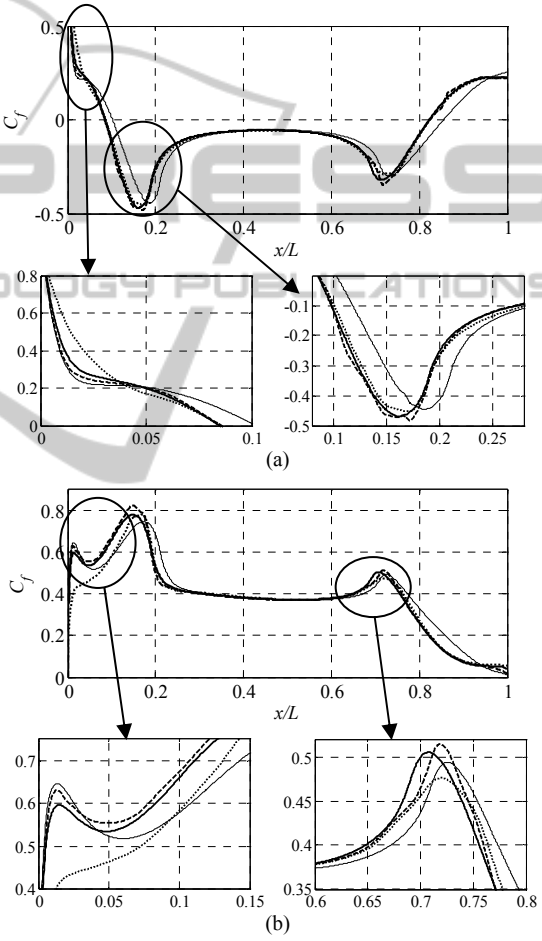

Figure 10: (a) Smoothened surrogate model (7)-(10) $C_{p.s}^{(i)}(\boldsymbol{x}^{(i)}) = C_{p.f}(\boldsymbol{x}^{(i)})$ (—), $C_{p.s}^{(i)}(\boldsymbol{x})$ (- - -), $C_{p.c}(\boldsymbol{x})$ (· · ·), and $C_{p.s}(\boldsymbol{x})$ (—); (b) Smoothened responses $C_{f.s}^{(i)}(\boldsymbol{x}^{(i)}) = C_{f.f}(\boldsymbol{x}^{(i)})$ (—), $C_{f.s}^{(i)}(\boldsymbol{x})$ (- - -), $C_{f.c}(\boldsymbol{x})$ (· · ·), and $C_{f.s}(\boldsymbol{x})$ (—).

where $I(X,Y,Z)$ is a function that interpolates the function values Y defined over the domain X onto the set Z. Here, we use cubic splines. In other words, the values of $A_{p.j}^{(i)}$ in the neighbourhood of $j_{\max}$ are "restored" using the values of $A_{p.j}^{(i)}$ from the surrounding of $j = j_{\max}-\Delta j, \ldots, j_{\max}+\Delta j$.

Figure 10(a) shows the "smoothened" surrogate model response corresponding to that of Fig. 9. Figure 10 shows the surrogate and the high-fidelity model responses, both C_p and C_f, at $\boldsymbol{x}^{(i)}$ and at some other design $\boldsymbol{x}$.

5 NUMERICAL EXAMPLES

5.1 General Setup

The proposed approach is applied to the hydrodynamic shape optimization of torpedo-type hulls, involving both the direct and inverse design approaches. Designs are obtained using the algorithm proposed in Section 4, where the surrogate model optimization is performed using the pattern-search algorithm (Koziel, 2010c). For comparison purposes, designs obtained through direct optimization of the high-fidelity model using the pattern-search algorithm (Koziel, 2010c) are also presented.

For both the direct and the inverse design approaches, the design variable vector is $\boldsymbol{x} = [a\ x_n\ y_n\ x_t\ y_t]^T$, where a is the nose length, (x_n,y_n) and (x_t,y_t) are the coordinates of the free control points on the nose and tail Bézier curves, respectively, i.e., points 3 and 8 in Fig. 2. See Section 2.1 for a description of the shape parameterization. The lower and upper bounds of design variables are $\boldsymbol{l} = [0\ 0\ 0\ 80\ 0]^T$ *cm* and $\boldsymbol{u} = [30\ 30\ 10\ 100\ 10]^T$ *cm*, respectively. Other geometrical shape parameters are, for both cases, L = 100 cm, d = 20 *cm,* and b = 50 *cm*. The flow speed is 2 *m*/*s* and the Reynolds number is 2 million.

5.2 Direct Design

Numerical results for a direct design case are presented in Table 1. The hull drag coefficient is minimized by finding the appropriate shape and length of the nose and tail sections for a given hull length, diameter, and cylindrical section length. In this case, the drag coefficient is reduced by 6.3%. This drag reduction comes from a reduction in skin friction and a lower pressure peak where the nose and tail connect with the midsection (Figs. 11(a) and 11(b)). These changes are due to a more streamlined nose (longer by 6 cm) and a fuller tail, when compared to the initial design (Fig. 11(c)).

Table 1: Numerical results for direct drag minimization. The flow speed is 2 *m*/*s* and the Reynolds number is 2 × 10^6. All the numerical values are from the high-fidelity model. N_c and N_f are the number of low- and high-fidelity model evaluations, respectively.

Variable	Initial	Pattern-search	This work
a	15.0000	21.8611	20.9945
x_n	5.0000	5.6758	5.6676
y_n	5.0000	2.7022	2.7531
x_t	90.0000	98.000	96.6701
y_t	5.0000	0.8214	3.0290
C_D	0.0915	0.0853	0.0857
N_c	N/A	0	300
N_f	N/A	282	3
Total cost	N/A	282	13

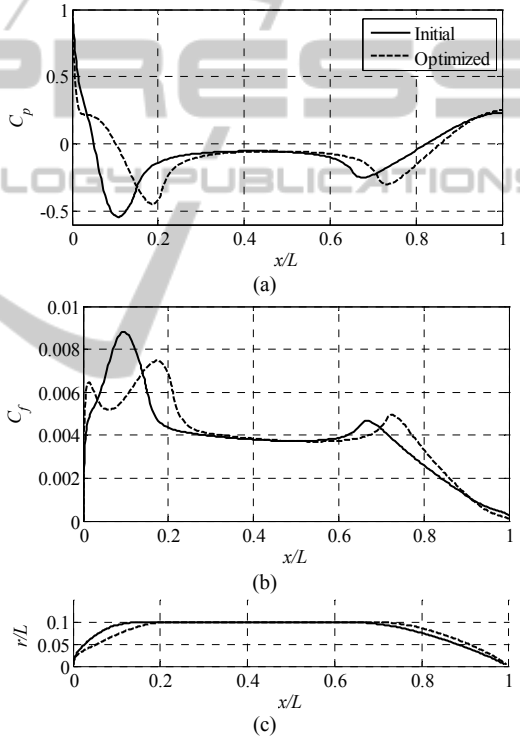

Figure 11: Direct hull drag minimization results showing initial and optimized (a) pressure distributions; (b) skin friction distributions; and (c) hull shapes.

The proposed method requires 3 high-fidelity and 300 low-fidelity model evaluations. The ratio of the high-fidelity model evaluation time to the corrected low-fidelity model evaluation time varies between 11 to 45, depending on whether the flow solver converges to the residual limit of 10^{-6}, or the maximum iteration limit of 1000. We express the total optimization cost of the proposed method in the equivalent number of high-fidelity model evaluations. For the sake of simplicity, we use a

fixed value of 30 as the high- to low-fidelity model evaluation time ratio. The results show that the total optimization cost of the proposed method is around 13 equivalent high-fidelity model evaluations. The direct optimization method, using the pattern-search algorithm (Koziel, 2010c), yields very similar design, but at the substantially higher computational cost of 282 high-fidelity model evaluations.

5.3 Inverse Design

Inverse design of the hull shape was performed by prescribing a target pressure distribution. The objective is to minimize the norm of the difference between the pressure distribution of the hull design and the target pressure distribution. The design variables and constraints are shown in Section 5.1.

The numerical results are of the inverse design are presented in Table 2. The proposed algorithm matched the target pressure distribution (the norm of the distributions is less than 2×10^{-5}) using less than 22 equivalent high-fidelity model evaluations. The direct optimization of the high-fidelity model using the pattern-search algorithm required 401 function calls to yield a comparable matching with the target.

Table 2: Numerical results for inverse design optimization with a target pressure distribution. N_c and N_f are the number of low- and high-fidelity model evaluations, respectively. F is the norm of the difference between the target and the design shapes.

Variable	Initial	Pattern-search	This work
A	18.000	24.7407	24.7667
x_n	7.0000	7.3704	6.8333
y_n	8.0000	4.7407	4.5667
x_t	85.0000	88.1111	88.6333
y_t	7.0000	5.5926	5.3000
F	0.0204	1.64E-5	1.93E-5
C_D	0.0925	0.0894	0.0893
N_c	N/A	0	500
N_f	N/A	401	5
Total cost	N/A	401	< 22

6 CONCLUSIONS

Computationally efficient simulation-driven multi-fidelity design optimization algorithm for axisymmetric hulls in incompressible fluid flow is presented. Our algorithm exploits a low-fidelity model, obtained through a coarse-discretization CFD simulation, and a response correction method, to construct a cheap and reliable surrogate of the fluid flow. The algorithm can be applied to both direct and inverse design approaches. We demonstrate that the optimized designs can be obtained at a low computational cost corresponding to a few high-fidelity CFD simulations.

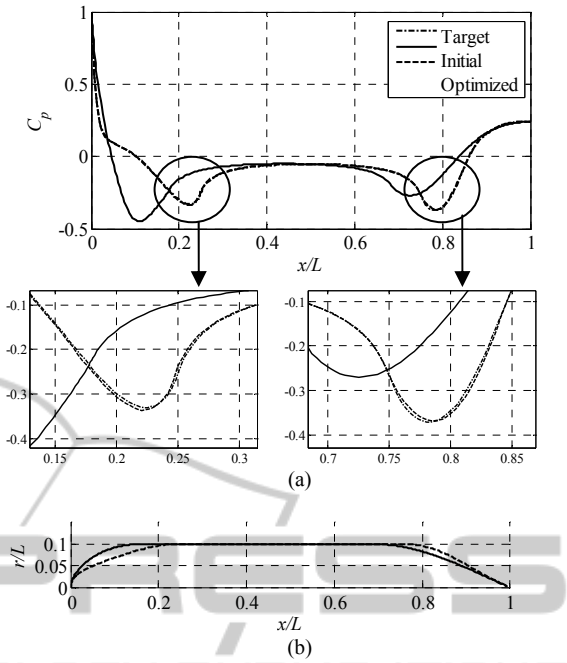

Figure 12: Results of the inverse design optimization with a prescribed target pressure distribution; (a) the target, initial, and optimized pressure distributions; (b) initial and optimized hull shapes.

REFERENCES

Allen, B., Vorus, W. S., and Prestero, T., 2000, Propulsion system performance enhancements on REMUS AUVs, In *Proceedings MTS/IEEE Oceans 2000*, September, Providence, Rhode Island.

Alexandrov, N. M., Lewis, R. M., Gumbert, C.R., Green, L. L., and Newman, P.A., 2000, Optimization with variable-fidelity models applied to wing design, *38th Aerospace Sciences Meeting & Exhibit*, Reno, NV, AIAA Paper 2000-0841.

Alexandrov, N. M., Lewis, R. M., 2001, An overview of first-order model management for engineering optimization. *Optimization and Engineering*. 2, 413-430.

Alvarez, A., Bertram, V., and Gualdesi, L., 2009, Hull hydrodynamic optimization of autonomous underwater vehicles operating at snorkelling depth, *Ocean Engineering*, vol. 36, pp. 105-112.

Bandler, J. W., Cheng, Q. S., Dakroury, S. A., Mohamed, A. S., Bakr, M.H., Madsen, K., and Søndergaard, J., 2004, Space Mapping: The State of The Art. *IEEE Trans. Microwave Theory Tech.*, 52(1), pp. 337-361.

Braembussche, R. A., 2008, Numerical Optimization for Advanced Turbomachinery Design, In *Optimization and Computational Fluid Dynamics*, Thevenin, D. and Janiga, G., editors, Springer, pp. 147-189.

Dalton, C., and Zedan, M. F., 1980, Design of low-drag axisymmetric shapes by the inverse method, *J. Hydronautics*, vol. 15, no. 1, pp. 48-54.

Dulikravich, G. S., 1991, Aerodynamic shape design and optimization, *29th AIAA Aerospace Sciences Meeting*, Reno, NV.

de Barros, E. A., Dantas, J. L. D., Pascoal, A. M., and de Sá, E., 2008, Investigation of normal force and moment coefficients for an auv at nonlinear angle of attack and sideslip angle, IEEE Journal of Oceanic Engineering, vol. 33, no. 4, pp. 538-549.

Echeverría, D., and Hemker, P.W., 2008, Manifold mapping: a two-level optimization technique. *Computing and Visualization in Science*. 11, pp. 193-206.

FLUENT, ver. 12.1, ANSYS Inc., Southpointe, 275 Technology Drive, Canonsburg, PA 15317, 2006.

Forrester, A.I.J., and Keane, A.J., 2009, Recent advances in surrogate-based optimization, *Progress in Aerospace Sciences*, vol. 45, no. 1-3, pp. 50-79.

Goldschmied, F.R., 1966, Integrated hull design, boundary-layer control, and propulsion of submerged bodies, *J. Hydronautics*, vol. 1, no. 1, pp. 2-11.

Huang, T. T., Liu, H. L., Groves, N. C., Forlini, T. J., Blanton, J. N., and Gowing, S., 1992, Measurements of flows over an axisymmetric body with various appendages (DARPA SUBOFF Experiments), In *Proceedings of the 19th Symposium on Naval Hydrodynamics*, Seoul, Korea.

ICEM CFD, ver. 12.1, ANSYS Inc., Southpointe, 275 Technology Drive, Canonsburg, PA 15317, 2006.

Jagadeesh, P., Murali, K., Idichandy, V.G., 2009, Experimental investigation of hydrodynamic force coefficients over auv hull form, *Ocean Engineering*, vol. 36, pp. 113-118.

Koziel, S., Bandler, J.W., and Madsen, K., 2006, A Space Mapping Framework for Engineering Optimization: Theory and Implementation. *IEEE Trans. Microwave Theory Tech*., 54(10), pp. 3721-3730.

Koziel, S., and Bandler, J.W., 2010a, Recent advances in space-mapping-based modeling of microwave devices. *International Journal of Numerical Modelling*, (23) 6, pp. 425-446

Koziel, S., 2010b, Shape-preserving response prediction for microwave design optimization. *IEEE Trans. Microwave Theory and Tech.*, 58(11), pp. 2829-2837.

Koziel, S., 2010c, Multi-fidelity multi-grid design optimization of planar microwave structures with Sonnet, *International Review of Progress in Applied Computational Electromagnetics*, Tampere, Finland, April 26-29, pp. 719-724.

Leifsson, L., and Koziel, S., 2010, Multi-fidelity design optimization of transonic airfoils using physics-based surrogate modeling and shape-preserving response prediction, *Journal of Computational Science*, vol. 1, no. 2, pp. 98-106.

Lepine, J., Guibault, F., Trepanier, J.-Y., and Pepin, F., 2001, Optimized nonuniform rational b-spline geometrical representation for aerodynamic design of wings, *AIAA Journal*, vol. 39, no. 11, pp. 2033-2041.

Lutz, Th., and Wagner, S., 1998, Numerical shape optimization of natural laminar flow bodies, In *Proceedings of the 21st ICAS Congress*, Sept. 13-18, Melbourne, Australia.

Myring, D.F., 1976, A theoretical study of body drag in subcritical axisymmetric flow, *Aeronautical Quarterly*, vol. 28, pp. 186-194.

Parsons, J.S., Goodson, R.E., and Goldschmied, F.R., 1974, Shaping of axisymmetric bodies for minimum drag in incompressible flow, *J. Hydronautics*, vol. 8, no. 3, pp. 100-107.

Queipo, N. V., Haftka, R. T., Shyy, W., Goel, T., Vaidynathan, R., and Tucker, P.K., 2005, Surrogate-Based Analysis and Optimization. *Progress in Aerospace Sciences*, 41(1), pp. 1-28.

Simpson, T. W., Peplinski, J., Koch, P.N., Allen, J.K., 2001, Metamodels for computer-based engineering design: survey and recommendations. Engineering with Computers. 17, pp. 129-150.

Solov'ev, S. A., 2009, Determining the shape of an axisymmetric body in a viscous incompressible flow on the basis of the pressure distribution on the body surface, *J. of Applied Mechanics and Technical Physics*, vol. 50, no. 6, pp. 927-935.

Søndergaard, J., 2003, Optimization using surrogate models – by the space mapping technique. Ph.D. Thesis, Informatics and Mathematical Modelling, Technical University of Denmark, Lyngby.

Tannehill, J.A., Anderson, D.A., and Pletcher, R.H., 1997, *Computational fluid mechanics and heat transfer*, 2nd edition, Taylor & Francis.

Yang, C., and Löhener, R., 2003, Prediction of flows over an axisymmetric body with appendages, *The 8th International Conference on Numerical Ship Hydrodynamics*, Sept. 22-25, Busan, Korea.

Yamamoto, I., 2007, Research and development of past, present, and future auv technologies, in *Proc. Int. Mater-class AUV Technol. Polar Sci. – Soc. Underwater Technol.*, Mar. 28-29, pp.17-26.